Metallacyclopropene Structures Identified by IRMPD Spectroscopic Investigation of the Dehydrogenation Reactions of Ta^+ and TaO^+ with Ethene

O. W. Wheeler,[†] R. A. Coates,[†] V. J. F. Lapoutre,[§] J. M. Bakker,[§]

and P. B. Armentrout[*,†]

[†]*Department of Chemistry, University of Utah, 315 S. 1400 E. Room 2020, Salt Lake City, Utah 84112, United States*

[§]*Radboud University, Institute for Molecules and Materials, FELIX Laboratory, Toernooiveld 7c, 6525ED Nijmegen, The Netherlands*

Abstract: Species formed in the reactions of Ta^+ and TaO^+ with ethene are examined spectroscopically using infrared multiple photon dissociation (IRMPD) action spectroscopy. Ta^+, $TaC_2H_2^+$, and TaO^+ are all observed to dehydrogenate ethene yielding $[Ta,2C,2H]^+$, $[Ta,4C,4H]^+$, and $[Ta,O,2C,2H]^+$, respectively. For these species, IR action spectra are obtained in the 225 – 3400 cm^{-1} range by monitoring fragmentation into the $[Ta,2C]^+$, $[Ta,4C,nH]^+$ (n = 2, 3), and $[Ta,O]^+$ mass channels, respectively. The spectra are assigned to $TaC_2H_2^+$, $Ta(C_2H_2)_2^+$, and $OTaC_2H_2^+$ metallacyclopropene species on the basis of comparisons with scaled vibrational spectra from B3LYP/def2-TZVPPD geometry optimized structures. To further elucidate the chemistry observed, complete reaction coordinate pathways having quintet, triplet, and singlet spin for all three dehydrogenation reactions have also been examined.

Keywords: action spectroscopy; CH bond activation; infrared multiple photon dissociation; potential energy surfaces; tantalum

1. Introduction

Finding efficient routes for the catalytic activation of CH bonds remains a topic at the forefront of industrial importance. Model gas-phase studies of this process began with the observations of Ridge and co-workers [1] and rapidly expanded [2]. In this work, a key concept, first noted by Clemmer et al. [3] and soon termed "two-state reactivity (TSR)" [4, 5], noted that the reactivity of transition metals with organic species could be enhanced by coupling between surfaces of different spin. Although these previous experimental explorations have elucidated the mechanisms and thermodynamics of a wide range of organometallic systems, there are few cases where definitive structural identifications of the products has been included [6-12]. The present study is designed to provide such identification using infrared multiple photon dissociation (IRMPD) action spectroscopy for the case of tantalum cations, a case where theory shows that TSR is fully operative.

The reaction of Ta^+ with a number of different hydrocarbons has been extensively investigated within the literature by both experimental [6, 8, 13-17] and computational [6, 8, 15, 17-20] approaches. Freiser and coworkers experimentally investigated the reaction of Ta^+ with a number of alkanes and characterized products formed through additional secondary collision-induced dissociation (CID) experiments [13]. They were the first to observe that Ta^+ reacts with the relatively inert methane molecule by dehydrogenation, forming $TaCH_2^+$, which reacts with up to an additional three methane molecules by dehydrogenation (eventually forming $[Ta,4C,8H]^+$. This observation was soon followed by similar studies of Irikura and Beachamp [14], and later by guided ion beam studies in our group [15]. Subsequent theoretical calculations showed that $Ta^+(^5F)$ can readily react with CH_4 to form a $Ta(CH_4)^+$ quintet intermediate, but the experimentally observed dehydrogenation process occurs only if a surface crossing to the triplet surface takes place [8, 15, 19]. This crossing leads to the slightly exothermic (-0.09 ± 0.03 eV) [15] formation of $TaCH_2^+(^3A'')$ + H_2 products through a dehydrogenation process [8, 15, 19].

Freiser and coworkers also observed that Ta^+ reacts with C_2H_6 at thermal energies to dehydrogenate yielding the $[Ta,2C,4H]^+$ species, which rapidly undergoes further

dehydrogenation to form $[Ta,2C,2H]^+$. The $[Ta,2C,4H]^+$ product had a 10% relative abundance, much less than the $[Ta,2C,2H]^+$ product with a relative abundance of 90%. Later, Gibson *et al.* reproduced these results obtaining a branching ratio of 20:80%. These authors also examined the reactions of Ta^+ and TaO^+ with C_2H_4, observing exclusive dehydrogenation to form $[Ta,2C,2H]^+$ and $[Ta,O,2C,2H]^+$, respectively, with efficiencies of 26% and 54%, respectively, of the collision limit.

Theoretical work by Lv *et al.* [20] investigated the reaction of $Ta^+(^5F, ^3F, ^1D) + C_2H_6$. This work specifically examined the spin-forbidden reaction mechanisms that allow for C-H and C-C bond activation by Ta^+ (even though the latter process is not observed experimentally). Their results indicate that exothermic formation of $TaC_2H_4^+ + H_2$ products requires a surface crossing between the reactant quintet surface and either the triplet or singlet surfaces. The lowest energy dehydrogenation process leads to the formation of $TaC_2H_4^+(^3B_1) + H_2(^1\Sigma_g^+)$ products (exothermic by 1.00 eV), with the singlet products, $^1A_1 + ^1\Sigma_g^+$, higher in energy by 0.47 eV. These authors have also theoretically examined the reaction of neutral Ta with C_2H_4, at the B3LYP/SDD/6-311++G(3df,3pd) level of theory [21]. This work again showed the importance of surface crossings in order for dehydrogenation to take place at or near thermal energies.

Spectroscopic characterization of the various species formed in the reactions of Ta^+ with hydrocarbons is limited. Simon *et al*. [6] experimentally examined the sequential reactions of Ta^+ with up to four methane molecules as well as ethane. One product of this study, $[Ta,2C,4H]^+$, was characterized by UV-visible photodissociation and H/D exchange coupled with density functional theory (DFT) calculations. These results indicated that the $[Ta,2C,4H]^+$ product structure was dependent on whether the reaction gas was methane or ethane, yielding what are likely to be a dihydridometallacyclopropene, $(H)_2TaC_2H_2^+$, and a metallacyclopropane, $c\text{-}TaC_2H_4^+$, cation, respectively. For the initial step in the reaction with methane, our groups have investigated a number of 5d transition metal cations exothermically reacting with CH_4 (or CD_4) to produce the MCH_2^+ (MCD_2^+) species, where $M^+ = Ta^+$, W^+, Os^+, Ir^+, and Pt^+ [8-10]. For the Ta^+ reaction, the $[Ta,C,2H]^+$ product was characterized as an agostically distorted $TaCH_2^+(^3A'')$ carbene structure,

which theory suggested could be formed exothermically (by 0.04 eV). It can be noted that Parke *et al*. [15] found an additional $^3A'$ structure only 0.032 eV higher in energy. Lapoutre *et al.* also noted that formation of a $^1A'$ state (also an agostically distorted Ta^+-carbene structure) could not be ruled out spectroscopically; however, its formation is endothermic by 0.37 eV according to theory.

The current work examines the reactions of $Ta^+ + x\ C_2H_4$, where x = 1 and 2, along with the reaction of $TaO^+ + C_2H_4$. The latter process was an unintentional but welcome consequence of adventitious O_2, water, or metal oxides within our experimental set-up. Products of these reactions were examined by IRMPD action spectroscopy and assigned structures with the aid of quantum chemical calculations. Theoretical work builds from the $Ta^+ + C_2H_6$ reaction coordinate pathways investigated computationally by Lv *et al*. [20] and the structures for $[Ta,2C,4H]^+$ examined by Simon *et al.* [6] These results also extend our previous IRMPD studies of products formed in the reactions of 5d transition metal cations with hydrocarbons, which include $M^+ + CH_4$ (M = Ta, W, Os, Ir, Pt) [8-10], and $M^+ + x\ CH_4$ (x = 1 – 4) (M = Ir, Pt) [11, 12].

2. Experimental and Computational Methods

2.1. Experiment

The present work used a Smalley-type laser ablation source[22-24] coupled to the Free-Electron Laser for IntraCavity Experiments (FELICE) at the Free Electron Lasers for Infrared eXperiments (FELIX) Laboratory in the Netherlands [25, 26]. The Ta^+ ions were produced by ablating a Ta rod with the second harmonic of a pulsed Nd:YAG laser (532 nm) in the presence of a burst of He gas, which cooled and translated the generated ions down a 3 mm diameter, 60 mm long channel. Exposure to reactant gas, C_2H_4, occurred ~50 mm downstream from the ablation source. Pulses of the initial He cooling/carrier gas and the reactant gases were adjusted such that minor amounts of products from the $Ta^+ + 2\ C_2H_4$ reactions were formed. After the initial reaction, the molecular beam underwent supersonic expansion into vacuum passing through a 2 mm diameter skimmer and a 0.45 mm slit aperture (both electrically grounded). Upon passing through

the skimmer and aperture, the beam entered an interaction region where IR irradiation occurred. The molecular beam crossed the laser beam at 35º and could be adjusted with respect to laser beam height and focal point, as previously described [25]. In the current work, IR radiation was generated in the 225 – 3400 cm^{-1} range. The radiation was transform limited with a spectral width at approximately 0.4% full-width at half-maximum (fwhm) of the central frequency. The laser macropulse was typically 5 μs in duration, consisted of picosecond-long micropulses at a 1 ns separation, and had energies typically in the 0.5 – 2 J range. After interacting with the IR laser, all ions in the molecular beam were extracted into a reflectron time-of-flight (RETOF) mass spectrometer (Jordan TOF Products, Inc.) to examine ion intensities as a function of mass-to-charge ratio. By operating the experiment at twice the IR laser repetition rate, two sets of mass spectra were generated in alternating fashion, yielding mass intensities $I_{sig}(v)$ with IR exposure at frequency v, and I_{ref} without IR exposure. IRMPD spectra were typically recorded by varying the IR frequency with 5 – 10 cm^{-1} step-sizes.

Two methods were used to further treat the experimental data: either depletion or growth processes. Depletion processes are a result of mass loss from species that have absorbed IR energy in excess of barriers for decomposition. The formula used to calculate the depletion yield was the negative logarithm of $I_{sig}(v)/I_{ref}$. Depletion spectra clearly stem from the mass in question, but are not background-free, and thus inherently noisy. If the fragment ion mass channel can be reliably established and is empty before irradiation, a better signal-to-noise spectrum can be determined through the fragmentation yield, calculated as $-\ln[I_{sig,P}/(I_{sig,P} + I_{sig,F} - I_{ref,F})]$, where P and F represent the precursor and fragment ions. The fragmentation yield spectrum was in all cases compared to the depletion spectrum to ascertain their consistency. For both types of spectra, corrections were performed for variation of the IR pulse energy across the wavenumber range examined.

2.2 Quantum Chemical Calculations

The present work utilized the Gaussian09 suite of programs [27] and was performed on the

workstations of the Center for High Performance Computing (CHPC) at the University of Utah. Comparisons are made between experimental spectra and vibrational frequencies derived from DFT geometry optimized structures. Geometries were optimized with the B3LYP hybrid functional [28, 29] and the def2-TZVPPD basis set [30], referred to in this work as "def2". The def2 basis set is a balanced triple-ζ valence basis set with double polarization and a diffuse function on all elements. It is an all-electron basis set for C and H atoms and a small-core (46 electron) effective core potential (ECP) for Ta [30], with the 5s, 5p, 6s, 6p, and 5d electrons explicitly treated. This approach was chosen because of our group's successful use in previous IRMPD spectroscopic studies concerning the reactions of 5d transition metal cations with methane and multiple methane reactant gases [8-12].

Additional test calculations were performed by comparing experimental energetics for different C_xH_y and Ta^+-C_xH_y systems to that determined by B3LYP/def2 and MP2(full)/def2 single-point energy calculations, using the B3LYP/def2 optimized geometries. Details are found in Table S1 of the Supplementary Material. Experimental results compared to B3LYP/def2 and MP2/def2 single point energies for the bond energies of both Ta^+-C_xH_y and C_xH_y systems had combined mean absolute deviations (MADs) of 0.12 eV and 0.35 eV, respectively. From these results, it is clear that B3LYP/def2 calculations more accurately predict this thermochemistry and are therefore the preferred calculations for this work. As discussed further below, we also calculated vibrational spectra for select isomers at the M06-2X/def2 and M06-L/def2 levels of theory for comparison with the B3LYP/def2 results. The M06-2X level of theory is a high-nonlocality functional with double the amount of nonlocal exchange (2X) and was chosen because of its accuracy for main group thermochemistry [31]. The M06-L local functional with 0% Hartree-Fock (HF) was chosen because of its accuracy concerning organometallic and inorganic systems [31].

To facilitate comparisons between experimental spectra and the theoretically predicted vibrational frequencies and IR intensities, the theoretical stick spectra were convoluted with a Gaussian line shape function having a width of 20 cm^{-1} (fwhm ≈ 45 cm^{-1}). A global frequency

scaling factor of 0.959 was used in the current work and found to best reproduce the experimental spectra. This scaling factor is used to specifically account for anharmonicity, red-shifting, and other deficiencies within the theoretical spectra associated with the absorption of multiple photons in the IRMPD process. In interpreting the previously obtained IRMPD spectra for $TaCH_2^+$, a similar scaling factor of 0.955 was used successfully [8].

3. Experimental Results

Laser vaporization of the tantalum sample in the molecular beam apparatus generates appreciable ion signals at *m/z* 181 and 197, corresponding to the monoisotopic Ta^+ and TaO^+. Exothermic and efficient formation of the tantalum oxide cation occurs readily in the reaction of $Ta^+(^5F)$ with O_2 (efficiency 100 ± 20% or 82 ± 25%)[32, 33] and with H_2O (efficiency 13 ± 4%) [34], and is essentially impossible to eliminate entirely. Introduction of ethene leads to intense signals at *m/z* 207, 223, and 233, which can be attributed to $[Ta,2C,2H]^+$, $[Ta,O,2C,2H]^+$, and $[Ta,4C,4H]^+$, consistent with previous studies [16]. Although the peak at *m/z* 223 could conceivably have the $[Ta,3C,6H]^+$ molecular formula, this product would correspond to the reaction $[Ta,2C,2H]^+ + C_2H_4 \rightarrow [Ta,3C,6H]^+ + C$, which is highly unlikely. Clearly, these assignments are further tested and validated by the spectroscopic studies detailed below.

Products formed in the reactions of Ta^+ and TaO^+ with C_2H_4 were examined with IRMPD spectroscopy in the 225 – 3400 cm^{-1} range. Upon irradiation, new ions are observed at *m/z* 205 (dehydrogenation of *m/z* 207) and *m/z* 231 (dehydrogenation of *m/z* 233) with additional signals from *m/z* 229, 230, and 232 observed at some wavelengths. Further, depletion of the *m/z* 223 and 233 channels was clearly observed. Figure S1 shows examples of mass spectra with (at 3000 cm^{-1}) and without IR exposure.

3.1. Spectrum of $[Ta,2C,2H]^+$

As shown in Figure 1, the fragmentation yield spectrum for $[Ta,2C]^+$ has three distinct bands located at 682, 1026, and 3070 cm^{-1}. (The relatively broad band at 3070 cm^{-1} probably

reflects the 0.5% fwhm bandwidth of FELICE, 15 cm^{-1} at 3000 cm^{-1}, coupled with nearly overlapping vibrational frequencies.) Both the 1026 and 3070 cm^{-1} bands have significantly lower intensities when compared to the band located at 682 cm^{-1}. A depletion spectrum for *m/z* 207 shows a comparable spectrum but is noisier. Thus, the $[Ta,2C]^+$ photoproduct is formed by dehydrogenation of $[Ta,2C,2H]^+$, a conclusion that can also be tested by comparing the $[Ta,2C]^+$ IRMPD spectrum with linear IR absorption spectra calculated for select $[Ta,2C,2H]^+$ isomers, Figure 1. Table 1 lists the relative energies of all seventeen species investigated and Figure S2 of the Supplementary Material shows their respective spectra. The three distinct bands of the $[Ta,2C]^+$ IRMPD spectrum are best reproduced by metallacyclopropene $Ta(C_2H_2)^+$ structures having C_{2v} symmetry. There are two of these structures, both $^3A_2$ and $^1A_1$ states with the latter 1.02 eV higher in energy (B3LYP/def2). The metallacyclopropene character of these species is evident from the CCH bond angles of 136° and 130°, respectively, rather than something closer to 180° characteristic of an acetylene adduct. The triplet ground state (GS) species matches the bands located at 1026 and 3070 cm^{-1} well, but also predicts a shoulder to the red of the 682 cm^{-1} band, which is not observed. Conversely, the singlet $TaC_2H_2^+$ species does a better job of reproducing the shape of the 682 cm^{-1} band, including its slight asymmetric line shape with a shoulder towards the blue, the 1026 cm^{-1} band is comparably reproduced, but the predicted peak at high frequencies is slightly blue shifted from experiment. A very weak band observed at 1395 cm^{-1} (shown as an inset in Figure 1) could support assignment to the triplet GS structure, which has a very weak mode (0.2 km/mol) predicted at 1354 cm^{-1}, whereas the singlet species has no such band. The frequency mismatch is, however, substantial, and the band could also be assigned to an overtone of the predicted 697 cm^{-1} band of the GS structure. Either way, we deem this weak band insufficient to fix assignment, and contributions from both of these species to the experimental spectrum seem plausible on the basis of the spectroscopy alone. The failure to observe strong theoretically predicted peaks in the 1100 – 2900 cm^1 range and below 600 cm^{-1} effectively rules out contributions from the $TaCCH_2^+(^3A_2)$, $HTaC_2H^+(^3A)$, and $HTaC_2H^+(^1A)$ structures (Figure 1) as well as higher lying species (Figure S2).

The character of the $TaC_2H_2^+$ vibrational modes for both the triplet and singlet states can be seen in Table 2 with a pictorial representation of the respective vibrational motions. For both species, the most intense band corresponds to the out-of-plane bend, mode 3. For the triplet species, the in-plane rocking motion, mode 2, is 50 cm^{-1} lower in frequency forming a shoulder to the red, whereas for the singlet species, mode 2 is 20 cm^{-1} higher than mode 3 forming a shoulder to the blue that better matches the experimental spectrum. The experimental band at 1026 cm^{-1} can be assigned to another in-plane rocking motion at nearly identical theoretical frequencies for both states. The experimental band at 3070 cm^{-1} is a superposition of the asymmetric and symmetric CH stretching modes. With the possible exception of the triplet 1354 cm^{-1} band discussed above, all other bands found theoretically have predicted intensities too small for observation.

In order to investigate whether the shape of the band at 682 cm^{-1} could be used more definitively to assign whether the triplet or singlet state of $TaC_2H_2^+$ is present, additional geometry optimizations and frequency calculations were performed at the M06-2X/def2 and M06-L/def2 levels of theory. These calculations predict that the singlet lies above the triplet by 1.02 eV for B3LYP, 1.07 eV for M06-2X, and only 0.65 eV for M06-L. The spectra from the M06-2X and M06-L levels of theory can be seen in Figure S3 of the Supplementary Material and required scaling factors of 0.949 and 0.932, respectively. All spectra are fairly similar, although the reproduction of experiment is poorer for the M06-L spectra compared to the B3LYP and M06-2X spectra. In all spectra, the rocking mode 2 remains red shifted compared to the out-of-plane bending mode 3 for the triplet species and blue shifted for the singlet species for all calculations. Thus, the character of the shapes of the 682 cm^{-1} band is not particularly sensitive to the level of theory. Further, we checked whether an anharmonic B3LYP/def2 calculation of the frequencies would change this behavior, but again the spectra obtained are similar and only the scaling factor needed changes (to 0.980).

3.2. Reaction Coordinate Pathways for the $Ta^+ + C_2H_4$ Reaction

Another means to assess whether the $[Ta,2C]^+$ growth spectrum might be assigned

preferentially to the triplet GS or higher energy singlet $TaC_2H_2^+$ metallacycle species is to examine the mechanisms and energetics for the formation of these species. Therefore, the $Ta^+ + C_2H_4$ reactions along quintet, triplet, and singlet spin surfaces were examined theoretically. The resulting reaction coordinate pathways (RCPs) are shown in Figure 2. Structures associated with the singlet and triplet pathways are displayed in Figure 3 with all relative energies listed in Table 3.

Beginning with the GS Ta^+ (^5F) + C_2H_4 reactants, an ethene adduct, $TaC_2H_4^+$ ^{5}**1**, is formed upon initial approach. Activation of a CH bond leads to the ^{5}TS**1/2** transition state followed by a hydrido tantalum vinyl cation, $HTaC_2H_3^+$ ^{5}**2**. Because this TS lies 0.18 eV above the reactants, efficient dehydrogenation at thermal energies cannot occur along the quintet surface. As a consequence, a surface crossing must occur to either the singlet or triplet surface in order for dehydrogenation to take place. Because of this, further calculations along the quintet surface were not conducted.

Along the triplet surface, the ethene adduct, ^{3}**1**, lies 2.19 eV lower in energy than the GS reactants. Because ^{3}**1** is 0.56 eV below ^{5}**1**, the crossing seam between the quintet and triplet states must occur in the entrance channel for reaction. This difference of 0.56 eV compares well with the 0.60 eV difference predicted by Maître and coworkers [6]. From ^{3}**1**, the transfer of a H atom to the Ta^+ occurs through ^{3}TS**1/2** and is 1.13 eV higher in energy than ^{3}**1**, but still 1.06 eV below the reactant asymptote. The ^{3}**2** intermediate has an asymmetrical $HTaC_2H_3^+$ structure with a ∠HTaCC dihedral angle of 105°. This species can rotate the Ta-H through ^{3}TS**2/3** (0.09 eV higher in energy) to form the planar $HTaC_2H_3^+$ structure, ^{3}**3**, having C_s symmetry and a ∠HTaCC dihedral angle of 0°. ^{3}TS**3/4** is a four-centered transition state that couples two hydrogen atoms and lies 0.21 eV higher in energy than ^{3}**3** while maintaining C_s symmetry. This forms a dihydrogen adduct of the triplet metallacyclopropene product ion, $(H_2)TaC_2H_2^+$ ^{3}**4**, which lies 1.88 eV below GS reactants. The final dehydrogenation step requires another 0.22 eV of energy and occurs through a loose transition state.

The singlet surface may also be populated after a surface crossing from the quintet surface. Like the triplet surface, this crossing must take place in the entrance channel because intermediate

^{1}**1** lies 0.12 eV below ^{5}**1**. The difference of 0.44 eV between singlet and triplet $TaC_2H_4^+$ structures matches the literature value of 0.47 eV from Lv *et al.* [20] This metallacyclopropane cation can then activate the CH bond over ^{1}TS**1/2**, the lowest energy pathway out of the $TaC_2H_4^+$ intermediates, 0.19 eV lower than ^{3}TS**1/2**. This leads to formation of $HTaC_2H_3^+$ ^{1}**2**, which lies 0.13 eV below its triplet analogue. Note that the low spin allows the metal center to bind to both carbons of the vinyl ligand, as well as the hydrogen ligand, which is approximately perpendicular to the plane established by TaCC. For further reaction, the singlet surface remains lower in energy than the triplet surface until the final dehydrogenation step. From ^{1}**2**, a second H atom is transferred to the metal center through ^{1}TS**2/5**, a process that requires only 0.24 eV. This process forms the $(H)_2TaC_2H_2^+$ intermediate, ^{1}**5**, a dihydride metallacyclopropene. Simon *et al.* previously identified this singlet species as the most stable of all $[Ta,2C,4H]^+$ species [6], consistent with Figure 2 and Table 3. The final dehydrogenation process involves H-H bond formation between the two hydride ligands. This subsequent H_2 loss occurs without any stable intermediates along the surface (e.g., the singlet state of $(H_2)TaC_2H_2^+$ was looked for by scanning the H-H bond distance but no stable intermediates were located before H_2 loss). It requires 1.02 eV more energy than the triplet dehydrogenation process, but still lies 0.64 eV below GS reactants. Note that the dehydrogenation mechanism differs on the triplet and singlet surfaces, but neither has any transition state in excess of the GS reactants. Thus, reaction along either surface is consistent with efficient dehydrogenation at thermal energies.

The subsequent dehydrogenation pathways of the singlet and triplet $TaC_2H_2^+$ dehydrogenation products can be seen in Figure 4 with structures shown in Figure 5. Table 3 lists energies of all species. For both singlet and triplet surfaces, the double dehydrogenation of ethene by Ta^+ is endothermic, which explains why the $[Ta,2C]^+$ channel is not populated in the absence of IR exposure. Along both spin surfaces, the first transition state, TS**6**, involves H transfer from the bound acetylene molecule to the Ta cation. The singlet pathway is slightly lower in energy (by 0.10 eV) than the triplet pathway, but this order inverts when the $HTaC_2H^+$ species forms, intermediate **6**, so that ^{3}**6** is lower than ^{1}**6** by 0.20 eV. Transfer of a second H atom occurs over

TS**6/7** with the singlet surface favored by 0.72 eV over ^{3}TS**6/7**. This action forms a dihydride **7** intermediate in which the two hydrogen ligands lie on the same side of the TaCC plane. Rotation of this plane through TS**7/7_0** leads to the **7_0** intermediate in which the two hydrogen ligands lie on opposite sides of the TaCC plane. On the triplet surface, the ^{3}**7_0** intermediate can also be formed directly from ^{3}**6** by passing over ^{3}TS**6/7_0**, but no similar transition state could be located on the singlet surface. On the triplet surface, ^{3}**7** can then evolve by passing over the rate-limiting ^{3}TS**7/8**, 2.77 eV above the $Ta^+ + C_2H_4$ reactants, which couples the two hydrogen ligands to form a dihydrogen ligand in the ^{3}**8** intermediate. Loss of H_2 to form the TaC_2^+ ($^3A''$) + H_2 products requires 0.39 eV. On the singlet surface, the ^{1}**7** dihydride intermediate loses H_2 (requiring 2.05 eV) without passing through a $(H_2)TaC_2^+$ intermediate. The TaC_2^+ ($^1A'$) + H_2 products lie 1.21 eV higher in energy than the TaC_2^+ ($^3A''$) + H_2 products.

3.3. Spectrum of the $[Ta,4C,4H]^+$ Product

The $[Ta,4C,4H]^+$ product at *m/z* 233 is formed by Ta^+ performing two dehydrogenations when reacting with 2 ethene molecules. Similar spectra were found for $[Ta,4C,4H]^+$ from both the depletion spectrum of the *m/z* 233 channel and a fragmentation yield spectrum recorded in the *m/z* = 231 and 230 channels. (Formation of *m/z* 230 is surprising as it must correspond to loss of H from the $[Ta,4C,2H]^+$ product corresponding to *m/z* 231; nevertheless, this product was clearly observed as shown in Figure S1. The nature of this product has not been further investigated.) The *m/z* 233 fragmentation yield spectrum is shown in Figure 6 and has five major bands with some lower intensity substructure. The most intense bands are a doublet located at 665 and 724 cm^{-1}. At 1016 cm^{-1}, there is a band that has three well-structured sidebands to the red (at 909, 922, and 976 cm^{-1}). Two additional bands are located at 1426 and 3076 cm^{-1}.

Figure 6 also shows a comparison of the fragmentation spectrum with theoretical spectra for various $[Ta,4C,4H]^+$ isomers. Table 4 lists the energies of all eight species found. Clearly, the $Ta(C_2H_2)_2^+$_C_{2v} ($^1A_1$) structure (with C_{2v} symmetry), the lowest energy isomer, provides the best spectroscopic match across the wavenumber range examined. This bis-metallacyclopropene

species has C_{2v} symmetry and its singlet state indicates the metal forms covalent bonds to all four carbons. In addition to reproducing the five major peaks, this species also has a small peak at 900 cm^{-1}, although it does a poor job of accounting for the sidebands in the 900 – 1000 cm^{-1} spectral range. Rather, we speculate that these are combination bands of the 258 cm^{-1} vibration with the triplet of bands predicted at 642, 664, and 718 cm^{-1}. This predicts bands at 900, 922 and 976 cm^{-1} compared to the experimental positions of 909, 933, and 977 cm^{-1}.

Vibrational motions of the $Ta(C_2H_2)_2^+\_C_{2v}$ ($^1A_1$) species, which are similar to those in Table 2, can be found in Table S2 of the Supplementary Material. Modes 4 – 21 are in-phase and out-of-phase combinations of the modes seen in Table 2 with shifts in frequencies ranging between -88 cm^{-1} (in-phase rocking motion of C_2H_2, mode 2 in Table 2) up to +338 cm^{-1} (in-phase C=C stretch, mode 7 of Table 2). At low frequencies, modes 1 – 3 are a scissoring motion between the two acetylene ligands (mode 1, 217 cm^{-1}) and at 241 cm^{-1} and 258 cm^{-1} the in-phase and out-of-phase twisting of the two Ta-acetylene ligands.

An alternative singlet $Ta(C_2H_2)_2^+\_C_s$ structure (with C_s symmetry) is 0.72 eV higher in energy but does a poor job of replicating the experimental spectrum from 500 – 800 cm^{-1} and can be ruled out. Likewise, the $Ta(C_2H_2)_2^+$ (^3A) species has predicted bands that do not appear in the experimental spectrum and lies 1.40 eV higher in energy than the ground structure. Additional metal-hydride species, $HTaC_2H(C_2H_2)^+$, were found with both singlet and triplet spins lying 0.85 and 2.15 eV above the ground structure. The ^1A structure can be ruled out because intense peaks predicted at 490, 1850, and 1980 cm^{-1} are not observed. The ^3A structure also does a poor job of replicating the experimental spectrum over the full wavenumber range examined.

3.4. Reaction Coordinate Pathway for $TaC_2H_2^+ + C_2H_4$.

Exploration of the reaction of $TaC_2H_2^+ + C_2H_4$ can be seen in the RCP shown in Figure 7 with structures in Figure 8. The relative energies for both the singlet and triplet surfaces are listed in Table 5. As noted above, the triplet state of $TaC_2H_2^+$ is lower in energy by 1.02 eV than the singlet state; however, complexation with C_2H_4 switches the order and the singlet surface becomes

the lowest energy pathway for the remainder of the dehydrogenation. On the singlet surface, intermediate ^{1}**9** goes through ^{1}TS**9/10** to form intermediate ^{1}**10,** $HTaC_2H_2(C_2H_3)^+$. This transition state is 1.30 eV higher in energy than intermediate ^{1}**9** but remains below the energy of the triplet GS $TaC_2H_2^+ + C_2H_4$ reactants by 0.70 eV. Intermediate ^{1}**10** then passes through the four-center ^{1}TS**10/11** in which the hydrogen atoms couple to form an H_2 ligand in intermediate ^{1}**11**, $(H_2)Ta(C_2H_2)_2^+$. This intermediate can readily dissociate by loss of the loosely bound H_2 molecule (0.27 eV) to form the final dehydrogenated $Ta(C_2H_2)_2^+$ ($^1A_1$) product lying 1.06 eV lower in energy than $TaC_2H_2^+(^3A_2) + C_2H_4$ GS reactants. Overall, these products lie 2.72 eV below $Ta^+(^5F)$ + 2 C_2H_4, explaining why they are readily formed.

The triplet surface parallels the singlet pathway after formation of intermediate ^{3}**9**, lying above ^{1}**9** by 0.77 eV. Here, the rate-limiting step at ^{3}TS**9/10** is found for CH bond activation (0.62 eV above the GS $TaC_2H_2^+ + C_2H_4$ reactants) and formation of the triplet products, $Ta(C_2H_2)_2^+(^3A'')$ + H_2, lies 0.34 eV higher in energy than the GS reactants. Relative to the $Ta^+(^5F)$ + 2 C_2H_4 reactants, the $Ta(C_2H_2)_2^+$ ($^3A''$) + 2 H_2 products lie 1.32 eV lower in energy, such that these species are also plausibly formed. The failure to observe these species indicates that the reaction system must be quenched to the lower energy singlet surface.

3.5. Spectrum of the $[Ta,O,C,2H]^+$ Product

The $[Ta,O,2C,2H]^+$ species at *m/z* 223 has a depletion spectrum that matches a growth spectrum at m/z 197 (loss of C_2H_2) and 221 (loss of H_2), with the latter a minor product channel. We here show the fragmentation yield spectrum based on loss of C_2H_2 in Figure 9. Because neither fragment channel is empty before irradiation, the signal to noise ratio of the data is somewhat poorer than the spectra in Figures 1 and 6. The spectrum contains at least three distinct bands and plausibly others. The main peaks include two strong absorbances at 665 and 992 cm^{-1} with a low intensity shoulder at 924 cm^{-1}, and a somewhat broader band centered at 3076 cm^{-1} In addition, there is a hint of a band at 1425 cm^{-1} barely coming out of the noise.

Table 6 lists the energies of all twelve $[Ta,O,2C,2H]^+$ species located and all theoretically

located species can be found in Figure S4. Figure 9 compares the experimental spectrum with select theoretical spectra. The lowest energy species is $OTaC_2H_2^+$ ($^1A'$), which is again a metallacyclopropene with the oxo ligand located nearly perpendicular to the TaCC plane, with a ∠OTaCC dihedral angle of 95°. This structure, shown in Figure 9, does the best job of replicating the experimental spectrum over the complete range examined, predicting a strong band at 659 cm^{-1} (symmetric out-of-plane CH bend), a doublet of intense peaks at 985 and 1001 cm^{-1} (TaO stretch and in-plane CH bends), and a doublet of CH stretches at 3061 and 3086 cm^{-1}. It also predicts a weak band at 1423 cm^{-1} (CC stretch) that nicely matches the very small intensity band observed at this frequency. The band observed at 924 cm^{-1} is not predicted well by a weak band at 869 (out-of-plane CH bend), and we conjecture that this may be a combination band of the intense 659 cm^{-1} band with the 263 (possibly 256) cm^{-1} band. For this species, the 12 vibrational modes are illustrated in Table S3 of the Supplementary Material. Most of the vibrations are analogous to those in Table 2, but modes 1, 2, and 8 involve the oxo ligand. These correspond to twisting of the acetylene group relative to the oxo ligand (256 cm^{-1}), scissoring of the O and C_2H_2 groups (263 cm^{-1}), and largely the Ta-O stretch (985 cm^{-1}). The other vibrations are shifted by -75 – 310 cm^{-1} from those shown in Table 2. The largest blue shift, +310 cm^{-1}, occurs for the C=C stretch (mode 7, Table 2), and the largest red shift, -75 cm^{-1}, is found for the rocking motion seen in mode 2 of Table 2.

The next lowest energy $[Ta,O,2C,2H]^+$ species, 0.63 eV higher in energy, is the $HTaO(C_2H)^+$ (^1A) species and can be ruled out because the predicted strong absorbance at 1890 cm^{-1}, a C-C stretch, is clearly absent from our experimental spectrum. The triplet $OTaC_2H_2^+$ species is 0.89 eV above its singlet analogue and is ruled out the basis of not observing the doublet of peaks at 3110 and 3190 cm^{-1} and the peak at 1780 cm^{-1}. The singlet and triplet metal-hydroxide species, $HOTaC_2H^+$, are 1.28 and 1.24 eV higher above the GS, respectively, and have spectra that also do a poor job of reproducing experiment.

3.6. Reaction Coordinate Pathway for $TaO^+ + C_2H_4$

The TaO^+ species has been examined theoretically by Hinton *et al.* and was found to have a $^3\Delta$ ground state with low-lying $^1\Delta$ and $^1\Sigma^+$ states 0.575 and 0.816 eV higher in energy for B3LYP/HW+/6-311+G(3df) calculations, respectively [35]. Given $D_0(TaO^+) = 7.10 \pm 0.12$ eV [32], formation of TaO^+ ($^3\Delta$) from the reactions of Ta^+ with O_2 and H_2O are exothermic by 1.98 ± 0.12 and 2.07 ± 0.12 eV, respectively, consistent with the efficiency of these reactions as studied previously [32-35]. Notably, this exothermicity also means that the singlet excited states are plausibly formed as well. RCPs for the $TaO^+ + C_2H_4$ reaction along singlet, triplet, and quintet surfaces were studied theoretically to elucidate the dehydrogenation process observed. The relative energies of all species investigated can be found in Table 7. The singlet and triplet RCPs can be seen in Figure 10 with structures in Figure 11. The quintet pathway is not shown because of the relatively high energies for all intermediates and transition states investigated.

The GS $TaO^+(^3\Delta)$ species readily complexes with C_2H_4 to form the ^{3}**12** intermediate, $OTaC_2H_4^+$, with a bond energy of 1.83 eV. Transfer of a H atom from the bound ethene ligand species occurs through ^{3}TS**12/13**, an energetically expensive process that is exothermic by only 0.02 eV. This leads to the ^{3}**13** intermediate, $HTaO(C_2H_3)^+$, which lies 0.18 eV lower in energy than the GS reactants. The rate-limiting transition state ^{3}TS**13/14** is 0.74 eV above GS reactants, and forms intermediate ^{3}**14**, $(H_2)TaO(C_2H_2)^+$. This species can then lose H_2 to form the final $OTaC_2H_2^+(^3A'')$ + H_2 products at -0.09 eV relative to the GS reactants. Overall, the high energy of ^{3}TS**13/14** explains why the $OTaC_2H_2^+(^3A'')$ species is not observed experimentally.

The singlet pathway starts with reactants that are 0.81 eV higher in energy than the GS triplet reactants. Complexation of C_2H_4 to the $TaO^+(^1\Delta)$ species forms the lowest-lying intermediate ^{1}**12** at -2.40 eV, 0.57 eV below ^{3}**12**. CH bond activation occurs through ^{1}TS**12/13** (at -1.17 eV) and forms intermediate ^{1}**13**, with a relative energy of -2.00 eV. A four-center transition state ^{1}TS**13/14** allows H-H bond formation (still 1.39 eV below GS reactants) and forms the ^{1}**14** intermediate lying 1.45 eV below GS reactants. The ^{1}**14** intermediate can lose H_2 through a loose transition state (requiring 0.46 eV) and forms the final $OTaC_2H_2^+$ ($^1A'$) + H_2 products in a reaction

exothermic by 0.99 eV. Clearly, there is a crossing between the triplet and singlet surfaces in the entrance channel for this reaction, such that the GS TaO^+ ($^3\Delta$) can react to form the $OTaC_2H_2^+$ ($^1A'$) product found spectroscopically. Alternatively, singlet excited states of TaO^+ formed exothermically in the initial reaction of Ta^+ with O_2 or H_2O can react along the singlet surface.

5. Conclusion

The current work examines the reactions of Ta^+, $TaC_2H_2^+$, and TaO^+ with C_2H_4. Using a combination of both experimental and theoretical work, structures of the resulting dehydrogenation products are successfully assigned. The $[Ta,2C,2H]^+$ species is assigned to a metallacyclopropene $TaC_2H_2^+$ structure with C_{2v} symmetry. The spectroscopic results are unable to definitively assign the experimental spectrum to either the triplet species or the higher-energy singlet species. Reaction of the $TaC_2H_2^+$ species with C_2H_4 readily forms a $[Ta,4C,4H]^+$ product, for which there is excellent agreement between experimental and theoretical results leading to assignment of the bis-metallacyclopropene $Ta(C_2H_2)_2^+$ ($^1A_1$) ground state structure. The $[Ta,O,2C,2H]^+$ product channel agrees best with the $OTaC_2H_2^+$ ($^1A'$) ground state species, and again has a metallacyclopropene structure. In all cases, theoretically determined reaction coordinate pathways validate the exothermic formation of each of these species from the reagents available in the experiment and suggest that two-state reactivity allows efficient formation of the observed products.

Associated Content

Supplementary Material

Table S1 is a comparison between experimental bond dissociation energies and both B3LYP/def2-TZVPPD and MP2(full)/def2-TZVPPD//B3LYP/def2-TZVPPD calculations. Tables S2 and S3 show vibrational modes for the lowest energy $Ta(C_2H_2)_2^+$ and $OTaC_2H_2^+$ structures. Figure S1 shows mass spectra with and without FELICE irradiation. Comparisons between all theoretical spectra examined and the experimental spectra for the $[Ta,2C,2H]^+$ and $[Ta,O,2C,2H]^+$ species can

be seen in Figures S2 and S4, respectively. Figure S3 compares spectra calculated at the B3LYP, M06-2X, and M06L levels of theory for singlet and triplet $TaC_2H_2^+$ species with the $[Ta,2C]^+$ fragment yield spectrum.

Author Information.

Corresponding Author

*P. B. A.: phone, +801-581-7885; e-mail, armentrout@chem.utah.edu.

Notes

The authors declare no competing financial interest.

Acknowledgement.

This work is supported by the National Science Foundation, Grants No. CHE-1664618 and OISE-1357887. We gratefully acknowledge the Nederlandse Organisatie voor Wetenschappelijk Onderzoek (NWO) for the support of the FELIX Laboratory. The Center for High Performance Computing (CHPC) at the University of Utah is acknowledged for their generous allocation of computing time.

References

[1] J. Allison, R.B. Freas, D.P. Ridge, Cleavage of alkanes by transition metal ions in the gas phase, J. Am. Chem. Soc., 101 (1979) 1332-1333.
[2] J. Roithová, D. Schröder, Selective Activation of Alkanes by Gas-Phase Metal Ions, Chem. Rev., 110 (2010) 1170–1211.
[3] D.E. Clemmer, Y.-M. Chen, F.A. Khan, P.B. Armentrout, State-Specific Reactions of $Fe^+(a^6D, a^4F)$ with D_2O and Reactions of FeO^+ with D_2, J. Phys. Chem., 98 (1994) 6522-6529.
[4] S. Shaik, D. Danovich, A. Fiedler, D. Schröder, H. Schwarz, Two-State Reactivity in Organometallic Gas-Phase Ion Chemistry, Helv. Chim. Acta, 78 (1995) 1393-1407.
[5] D. Schröder, S. Shaik, H. Schwarz, Two-state Reactivity as a New Concept in Organometallic Chemistry, Acc. Chem. Res., 33 (2000) 139-145.
[6] A. Simon, L. MacAleese, P. Boissel, P. Maître, Towards the Characterization of the Mechanism of the Sequential Activation of Four Methane Molecules by Ta^+, Int. J. Mass Spectrom., 219 (2002) 457-473.

[7] A. Simon, J. Lemaire, P. Boissel, P. Maître, Competition Between Agostic WCH_2^+ and $HWCH^+$: A Joint Experimental and Theoretical Study J. Chem. Phys., 115 (2001) 2510-2518.
[8] V.J.F. Lapoutre, B. Redlich, A.F.G. van der Meer, J. Oomens, J.M. Bakker, A. Sweeney, A. Mookherjee, P.B. Armentrout, Structures of the Dehydrogenation Products of Methane Activation by 5d Transition Metal Cations, J. Phys Chem. A, 117 (2013) 4115-4126.
[9] C.J. Owen, G.C. Boles, V. Chernyy, J.M. Bakker, P.B. Armentrout, Structures of the Dehydrogenation Products of Methane Activation by 5d Transition Metal Cations Revisited: Deuterium Labeling and Rotational Contours, J. Chem. Phys., 148 (2018) 044307.
[10] P.B. Armentrout, S. Kuijpers, O. Lushchikova, R.L. Hightower, G.C. Boles, J.M. Bakker, Spectroscopic Identification of the Carbyne Hydride Structure of the Dehydrogenation Product of Methane Activation by Osmium Cations, J. Am. Soc. Mass Spectrom., 29 (2018) 1781-1791.
[11] O.W. Wheeler, M. Salem, A. Gao, J.M. Bakker, P.B. Armentrout, Activation of C-H bonds in $Pt^+ + xCH_4$ Reactions, where x = 1 – 4: Identification of the Platinum Dimethyl Cation, J. Phys. Chem. A, 120 (2016) 6216–6227.
[12] O.W. Wheeler, M. Salem, A. Gao, J.M. Bakker, P.B. Armentrout, Sequential Activation of Methane by Ir^+: An IRMPD and Theoretical Investigation, Int. J. Mass Spectrom., 435 (2019) 78-92.
[13] S.W. Buckner, T.J. MacMahon, G.D. Byrd, B.S. Freiser, Gas-Phase Reactions of Nb^+ and Ta^+ with Alkanes and Alkenes. C-H Bond Activation and Ligand-Coupling Mechanisms, Inorg. Chem., 28 (1989) 3511-3518.
[14] K.K. Irikura, J.L. Beauchamp, Methane Oligomerization in the Gas Phase by Third-Row Transition-Metal Ions, J. Am. Chem. Soc., 113 (1991) 2769-2770.
[15] L.G. Parke, C.S. Hinton, P.B. Armentrout, Experimental and Theoretical Studies of the Activation of Methane by Ta^+ and the Bond Energies of Ta^+-CH_x (x = 1 - 3), J. Phys. Chem. C, 111 (2007) 17773-17787.
[16] J.K. Gibson, R.G. Haire, J. Marçalo, M. Santos, A. Pires de Matos, M.K. Mrozik, R.M. Pitzer, B.E. Bursten, Gas-Phase Reactions of Hydrocarbons with An^+ and AnO^+ (An = Th, Pa, U, Np, Pu, Am, Cm): The Active Role of 5f Electrons in Organoprotactinium Chemistry, Organomet., 26 (2007) 3947-3956.
[17] P.B. Armentrout, Methane Activation by 5d Transition Metals: Energetics, Mechanisms, and Periodic Trends, Chem.: Eur. J. , 23 (2017) 10-18.
[18] K.K. Irikura, W.A. Goddard III, Energetics of Third-Row Transition Metal Methylidene Ions MCH_2^+ (M = La, Hf, Ta, W, Re, Os, Ir, Pt, Au), J. Am. Chem. Soc., 116 (1994) 8733-8740.
[19] N. Sandig, W. Koch, Mechanism of the Ta^+-Mediated Activation of the C-H Bond in Methane, Organomet., 16 (1997) 5244-5251.
[20] L.-L. Lv, Y.-C. Wang, Z.-Y. Geng, Y.-B. Si, Q. Wang, H.-W. Liu, Activation of C_2H_6 by Gas-Phase Ta^+: Potential Energy Surfaces, Spin−Orbit Coupling, Spin-Inversion Probabilities, and Reaction Mechanisms, Organomet., 28 (2009) 6160-6170.
[21] C.-L. Wang, Y.-C. Wang, Y.-Z. Jin, D.-F. Ji, M.-J. La, W.-P. Ma, J.-Y. Nian, Theoretical Study of Activation of the C–H Bond in C_2H_4 by the Group 5 Metal Atoms (V, Nb, Ta) in the Gas-Phase, Comp. Theo. Chem., 974 (2011) 43-51.
[22] T.G. Dietz, M.A. Duncan, D.E. Powers, R.E. Smalley, Laser Production of Supersonic Metal Cluster Beams, J. Chem. Phys., 74 (1981) 6511-6512.
[23] V.E. Bondybey, J.H. English, Laser Induced Fluorescence of Metal Clusters Produced by Laser Vaporization: Gas Phase Spectrum of Pb_2, J. Chem. Phys., 74 (1981) 6978-6979.
[24] M.A. Duncan, Laser Vaporization Cluster Sources, Rev. Sci. Instrum., 83 (2012) 041101.

[25] J.M. Bakker, V.J.F. Lapoutre, B. Redlich, J. Oomens, B.G. Sartakov, A. Fielicke, G. von Helden, G. Meijer, A.F.G. van der Meer, Intensity-resolved IR Multiple Photon Ionization and Fragmentation of C_{60}, J. Chem. Phys., 132 (2010) 074305.
[26] M. Haertelt, V.J.F. Lapoutre, J.M. Bakker, B. Redlich, A. Fielicke, G. Meijer, Structure Determination of Anionic Metal Clusters via Infrared Resonance Enhanced Multiple Photon Electron Detachment Spectroscopy, J. Phys. Chem. Lett., 2 (2011) 1720-1724.
[27] M.J. Frisch, G.W. Trucks, H.B. Schlegel, G.E. Scuseria, M.A. Robb, J.R. Cheeseman, G. Scalmani, V. Barone, B. Mennucci, G.A. Petersson, H. Nakatsuji, M. Caricato, X. Li, H.P. Hratchian, A.F. Izmaylov, J. Bloino, G. Zheng, J.L. Sonnenberg, M. Hada, M. Ehara, K. Toyota, R. Fukuda, J. Hasegawa, M. Ishida, T. Nakajima, Y. Honda, O. Kitao, H. Nakai, T. Vreven, J.A. Montgomery Jr., J.E. Peralta, F. Ogliaro, M.J. Bearpark, J. Heyd, E.N. Brothers, K.N. Kudin, V.N. Staroverov, R. Kobayashi, J. Normand, K. Raghavachari, A.P. Rendell, J.C. Burant, S.S. Iyengar, J. Tomasi, M. Cossi, N. Rega, N.J. Millam, M. Klene, J.E. Knox, J.B. Cross, V. Bakken, C. Adamo, J. Jaramillo, R. Gomperts, R.E. Stratmann, O. Yazyev, A.J. Austin, R. Cammi, C. Pomelli, J.W. Ochterski, R.L. Martin, K. Morokuma, V.G. Zakrzewski, G.A. Voth, P. Salvador, J.J. Dannenberg, S. Dapprich, A.D. Daniels, Ö. Farkas, J.B. Foresman, J.V. Ortiz, J. Cioslowski, D.J. Fox, Gaussian 09, Revision D.01 in, Gaussian, Inc., Wallingford, CT, USA, 2009.
[28] C. Lee, W. Yang, R.G. Parr, Development of the Colle-Salvetti Correlation-Energy Formula into a Functional of the Electron Density, Phys. Rev. B, 37 (1988) 785-789.
[29] A.D. Becke, Density-functional Thermochemistry. III. The Role of Exact Exchange, J. Chem. Phys., 98 (1993) 5648-5652.
[30] F. Weigend, R. Ahlrichs, Balanced basis sets of split valence, triple zeta valence and quadruple zeta valence quality for H to Rn: Design and assessment of accuracy, Phys. Chem. Chem. Phys., 7 (2005) 3297-3305.
[31] Y. Zhao, D.G. Truhlar, The M06 Suite of Density Functionals for Main Group Thermochemistry, Thermochemical Kinetics, Noncovalent Interactions, Excited States, and Transition Elements: Two New Functionals and Systematic Testing of Four M06-Class Functionals and 12 Other Functionals, Theor. Chem. Acc., 120 (2008) 215-241.
[32] C.S. Hinton, F.-X. Li, P.B. Armentrout, Reactions of Hf^+, Ta^+, and W^+ with O_2 and CO: Metal Carbide and Metal Oxide Cation Bond Energies, Int. J. Mass Spectrom., 280 (2009) 226-234.
[33] G.K. Koyanagi, D. Caraiman, V. Blagojevic, D.K. Bohme, Gas-Phase Reactions of Transition-Metal Ions with Molecular Oxygen: Room-Temperature Kinetics and Periodicities in Reactivity, J. Phys. Chem. A, 106 (2002) 4581-4590.
[34] P. Cheng, G.K. Koyanagi, D.K. Bohme, Heavy Water Reactions with Atomic Transition-Metal and Main-Group Cations: Gas Phase Room-Temperature Kinetics and Periodicities in Reactivity, J. Phys. Chem. A, 111 (2007) 8561-8573.
[35] C.S. Hinton, M. Citir, M. Manard, P.B. Armentrout, Collision-induced Dissociation of MO^+ and MO_2^+ (M = Ta and W): Metal Oxide and Dioxide Cation Bond Energies, Int. J. Mass Spectrom., 308 (2011) 265-274.

Table 1. Relative energies (in eV) for $[Ta,2C,2H]^+$ structures at 0 K.[a]

Molecular Formula	Spin =	1		3		5
$[Ta,2C,2H]^+$	State	B3LYP[b]	State	B3LYP[b]	State	B3LYP[b]
$TaC_2H_2^+$	$^1A_1$	1.02	$^3A_2$	0.00	$^5B_2$	1.57
$TaCCH_2^+$	$^1A_1$	1.54	$^3A_2$	1.16	$^5B_2$	1.87
$HTaC_2H^+$	^1A	1.59	^3A	1.39	$^5A''$	4.05
$(H)_2TaC_2^+$_∠HTaH>90°	$^1A'$	2.75	$^3A'$	3.89	$^5A_2$	6.29
$(H)_2TaC_2^+$_∠HTaH<90°	$^1A'$	2.99	$^3A''$	4.07		–
$Ta(CH)_2^+$	$^1A_1$	5.07	$^3B_1$	4.57	$^5A_1$	3.77

[a] Geometries optimized at the B3LYP/def2-TZVPPD level of theory. The "–" symbol indicates the failure to locate an intermediate for the designated structure and spin state. [b] B3LYP/def2-TZVPPD single point energies with zero-point energy corrections.

Table 2. Vibrational modes and respective intensities for the $TaC_2H_2^+$ ($^3A_2$, $^1A_1$) species.[a]

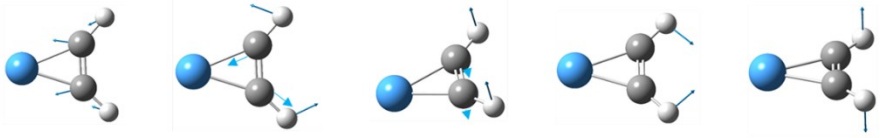

State	Mode	1	2	3	4	5
$^3A_2$	Frequency (cm^{-1})	575	649	697	788	895
	Intensity (km/mol)	3.0	21.5	82.4	1.1	0.0
$^1A_1$	Frequency (cm^{-1})	449	702	682	740	767
	Intensity (km/mol)	3.9	54.2	138.2	6.0	0.0

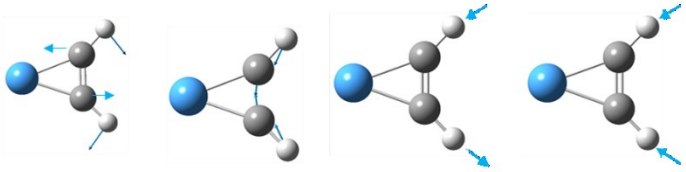

State	Mode	6	7	8	9
$^3A_2$	Frequency (cm^{-1})	1036	1354	3059	3080
	Intensity (km/mol)	74.5	0.2	27.6	41.3
$^1A_1$	Frequency (cm^{-1})	1034	1113	3077	3091
	Intensity (km/mol)	46.6	0.0	39.4	68.0

[a] Displacement vectors shown from Gaussian output file with additional vectors added to illustrate motions that were overlapped by solid atom spheres. Modes shown for the lower energy triplet species. Mode 1 of the singlet species differs slightly and has the H vectors pointed toward each other. All frequencies scaled by 0.959.

Table 3. Relative energies (in eV) for $Ta^+ + C_2H_4$ reaction coordinate pathways.[a]

	Spin =	1	3		5	
Species	State	B3LYP	State	B3LYP	State	B3LYP
$Ta^+ + C_2H_4$	^1D	0.56	^3P	0.37	^5F	0.00
$TaC_2H_4^+$ (**1**)	$^1A_1$	-1.75	$^3A_2$	-2.19	$^5A_2$	-1.63
TS**1/2**	^1A	-1.25	^3A	-1.06	^5A	0.18
$HTaC_2H_3^+$ (**2**)	^1A	-2.09	^3A	-1.96	^5A	-0.12
TS**2/3**		–	^3A	-1.85		
$HTaC_2H_3^+$_C_s (**3**)		–	$^3A''$	-1.90		
TS**3/4**		–	$^3A''$	-1.69		
$(H_2)TaC_2H_2^+$ (**4**)		–	$^3A''$	-1.88		
TS**2/5**	^1A	-1.85		–		
$(H)_2TaC_2H_2^+$ (**5**)	$^1A'$	-2.82		–		
$TaC_2H_2^+ + H_2$	$^1A_1$	-0.64	$^3A_2$	-1.66		
TS**6** + H_2	^1A	0.82	^3A	0.92		
$HTaC_2H^+$ (**6**)+ H_2	^1A	-0.07	^3A	-0.27		
TS**6/7** + H_2	^1A	1.84	^3A	2.56		
$(H)_2TaC_2^+$ (**7**) + H_2	$^1A'$	1.33	$^3A'$	2.41		
TS**7/8**		–	^3A	2.77		
$(H_2)TaC_2^+$ (**8**) + H_2		–	$^3A'$	1.78		
$TaC_2^+ + 2\ H_2$	$^1A'$	3.38	$^3A''$	2.17		
TS**6/7_0** + H_2			^3A	2.36		
$(H)_2TaC_2^+$ (**7_0**) + H_2	$^1A'$	1.09	$^3A'$	2.23		
TS**7/7_0**	^1A	1.46	^3A	2.48		

[a] Geometries and energies (including zero-point energy corrections) optimized at the B3LYP/def2-TZVPPD level of theory. The "–" symbol indicates the failure to locate an intermediate for the designated structure and spin state.

Table 4. Relative energies (in eV) for $[Ta,4C,4H]^+$ structures at 0 K.[a]

Molecular Formula	Spin =	1		3		5
$[Ta,4C,4H]^+$	State	B3LYP	State	B3LYP	State	B3LYP
$Ta(C_2H_2)_2^+\_C_{2v}$	$^1A_1$	0.00		–		–
$Ta(C_2H_2)_2^+\_C_s$	$^1A'$	0.72		–	$^5A''$	2.66
$Ta(C_2H_2)_2^+$		–	^3A	1.40		–
$HTaC_2H(C_2H_2)^+$	^1A	0.85	^3A	2.15		–
$TaC_2(C_2H_4)^+$	$^1A'$	2.59		–	^5A	4.69

[a] Geometries and energies (including zero-point energy corrections) optimized at the B3LYP/def2-TZVPPD level of theory. The "–" symbol indicates the failure to locate an intermediate for the designated structure and spin state.

Table 5. Relative energies (in eV) for $TaC_2H_2^+ + C_2H_4$ reaction coordinate pathways.[a]

	Spin = 1		3	
Species	State	B3LYP	State	B3LYP
$TaC_2H_2^+ + C_2H_4$	$^1A'$	1.02	$^3A_2$	0.00
$TaC_2H_2(C_2H_4)^+$ (**9**)	^1A	-2.00	^3A	-1.23
TS**9/10**	^1A	-0.70	^3A	0.62
$HTaC_2H_2(C_2H_3)^+$ (**10**)	^1A	-1.90	^3A	0.16
TS**10/11**	^1A	-1.19	^3A	0.01
$(H_2)Ta(C_2H_2)_2^+$ (**11**)	^1A	-1.33	^3A	-0.02
$Ta(C_2H_2)_2^+ + H_2$	^1A	-1.06	^3A	0.34

[a] Geometries and energies (including zero-point energy corrections) optimized at the B3LYP/def2-TZVPPD level of theory.

Table 6. Relative energies (in eV) for $[Ta,O,2C,2H]^+$ structures at 0 K.[a]

Molecular Formula	Spin =	1		3		5
$[Ta,O,2C,2H]^+$	State	B3LYP	State	B3LYP	State	B3LYP
$OTaC_2H_2^+$	$^1A'$	0.00	$^3A''$	0.89	^5A	4.31
$HTaO(C_2H)^+$	^1A	0.63	^3A	3.11	^5A	6.42
$HOTa(C_2H)^+$	^1A	1.28	^3A	1.24	$^5A''$	4.25
$HTaOH(C_2)^+$	^1A	2.36	^3A	3.48	^5A	6.25

[a] Geometries and energies (including zero-point energy corrections) optimized at the B3LYP/def2-TZVPPD level of theory.

Table 7. Relative energies (in eV) for $TaO^+ + C_2H_4$ reaction coordinate pathways.[a]

	Spin =	1		3		5
Species	State	B3LYP	State	B3LYP	State	B3LYP
$TaO^+ + C_2H_4$	$^1\Delta$	0.81	$^3\Delta$	0.00	$^5\Pi$	3.49
$OTaC_2H_4^+$ (**12**)	$^1A'$	-2.40	$^3A''$	-1.83	^5A	1.48
TS**12/13**	^1A	-1.17	^3A	-0.02		–
$HTaO(C_2H_3)^+$ (**13**)	^1A	-2.00	^3A	-0.18	^5A	2.43
TS**13/14**	^1A	-1.39	^3A	0.74	^5A	3.52
$(H_2)TaO(C_2H_2)^+$ (**14**)	^1A	-1.45	$^3A''$	-0.48	^5A	2.82
$OTaC_2H_2^+ + H_2$	$^1A'$	-0.99	$^3A''$	-0.09	^5A	3.32

[a] Geometries and energies (including zero-point energy corrections) optimized at the B3LYP/def2-TZVPPD level of theory. The "–" symbol indicates the failure to locate an intermediate for the designated structure and spin state.

Figure Captions

Fig. 1. IRMPD fragmentation yield spectrum for $[Ta,2C]^+$ (in shade) with vibrational spectra from select B3LYP/def2-TZVPPD geometry optimized $[Ta,2C,2H]^+$ isomers. State and relative energies shown from B3LYP (red) and MP2(full) (blue) zero-point energy corrected single point energy calculations. In all panels, the experimental spectra above 900 cm^{-1} have been multiplied by a factor of five and in the top panel, the inset shows another multiplication of 10.

Fig. 2. Reaction coordinate pathway for the singlet (red), triplet (dashed blue), and quintet (dark green) surfaces of $Ta^+ + C_2H_4$. Geometry optimizations and single point energy calculations were performed at the B3LYP/def2-TZVPPD level of theory and include zero-point energy corrections.

Fig. 3. B3LYP/def2-TZVPPD geometry optimized structures from the singlet and triplet reaction pathways shown in Figure 2.

Fig. 4. Reaction coordinate pathway for the singlet (red) and triplet (dashed blue) surfaces of $TaC_2H_2^+$ undergoing dehydrogenation. Geometry optimizations and single point energy calculations were performed at the B3LYP/def2-TZVPPD level of theory and include zero-point energy corrections.

Fig. 5. B3LYP/def2-TZVPPD geometry optimized structures from the singlet reaction pathways shown in Figure 4.

Fig. 6. IRMPD fragmentation yield spectrum for $[Ta,4C,2H]^+$ (in shade) with vibrational spectra from B3LYP/def2-TZVPPD geometry optimized $[Ta,4C,4H]^+$ isomers. State and relative energies shown from B3LYP (red) and MP2(full) (blue) zero-point energy corrected single point energy calculations.

Fig. 7. Reaction coordinate pathway for the singlet (red) and triplet (dashed blue) surfaces of $TaC_2H_2^+ + C_2H_4$. Geometry optimizations and single point energy calculations were performed at the B3LYP/def2-TZVPPD level of theory and include zero-point energy corrections. Dotted line represents the energy associated with $Ta^+ (^5F) + 2C_2H_4 - H_2$.

Fig. 8. B3LYP/def2-TZVPPD geometry optimized structures from the singlet reaction pathways shown in Figure 7.

Fig. 9. IRMPD fragmentation yield spectrum for $[Ta,O]^+$ (in shade) with vibrational spectra from select B3LYP/def2-TZVPPD geometry optimized $[Ta,O,2C,2H]^+$ isomers. Relative energies shown from B3LYP (red) and MP2(full) (blue) zero-point energy corrected single point energy calculations. Inset in top panel shows part of the theoretical and experimental spectra multiplied by a factor of ten.

Fig. 10. Reaction coordinate pathway for the singlet (red) and triplet (dashed blue) surfaces of $TaO^+ + C_2H_4$. Geometry optimizations and single point energy calculations were performed at the B3LYP/def2-TZVPPD level of theory and include zero-point energy corrections.

Fig. 11. B3LYP/def2-TZVPPD geometry optimized structures from the singlet reaction pathways shown in Figure 10.

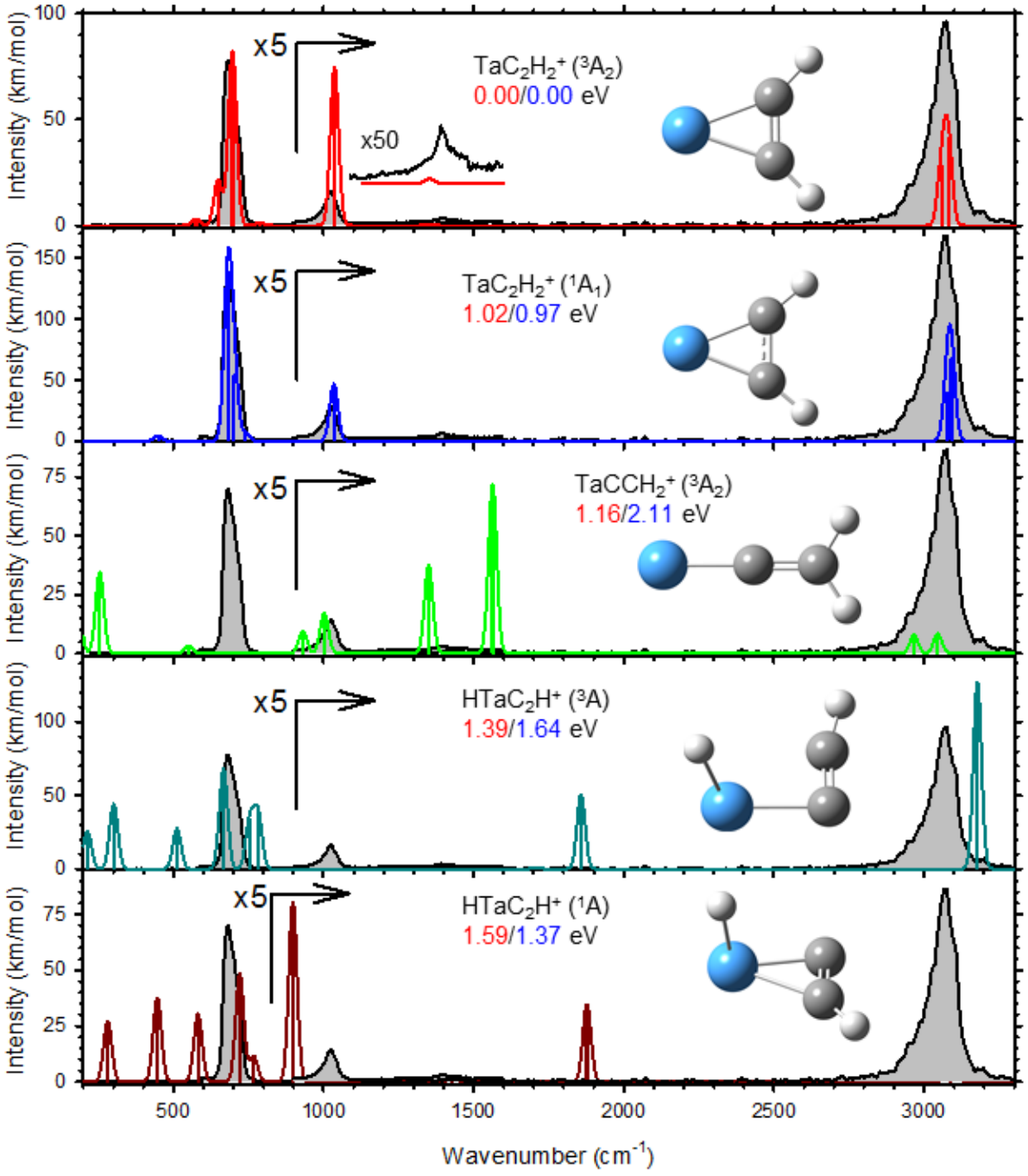
Intensity (km/mol)
x5
x50
TaC2H2+ (3A2)
0.00/0.00 eV
TaC2H2+ (1A1)
1.02/0.97 eV
TaCCH2+ (3A2)
1.16/2.11 eV
HTaC2H+ (3A)
1.39/1.64 eV
HTaC2H+ (1A)
1.59/1.37 eV
Wavenumber (cm-1)

Figure 1

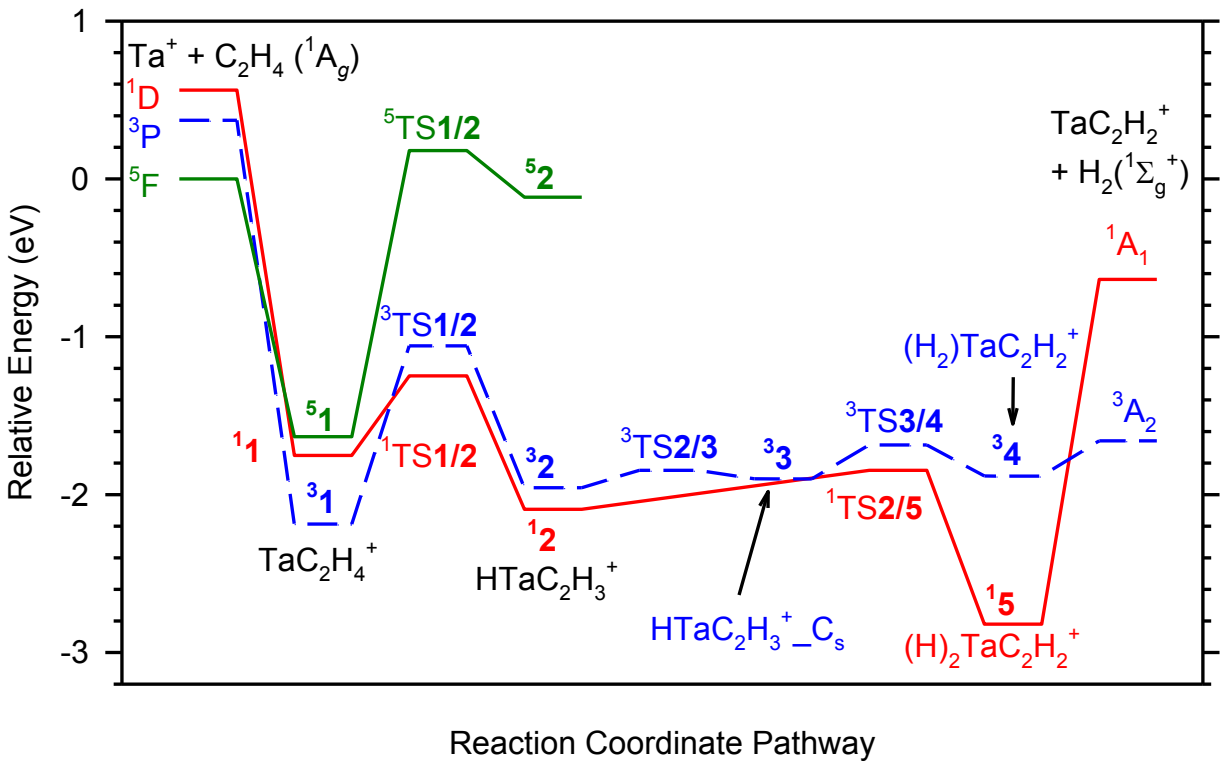
Ta+ + C2H4 (1Ag)
1D
3P
5F
5TS1/2
52
TaC2H2+
+ H2(1Σg+)
1A1
3TS1/2
(H2)TaC2H2+
51
3A2
3TS3/4
11
1TS1/2
32
3TS2/3
33
34
31
1TS2/5
TaC2H4+
12
HTaC2H3+
HTaC2H3+_Cs
15
(H)2TaC2H2+
Relative Energy (eV)
Reaction Coordinate Pathway
1
0
-1
-2
-3

Figure 2

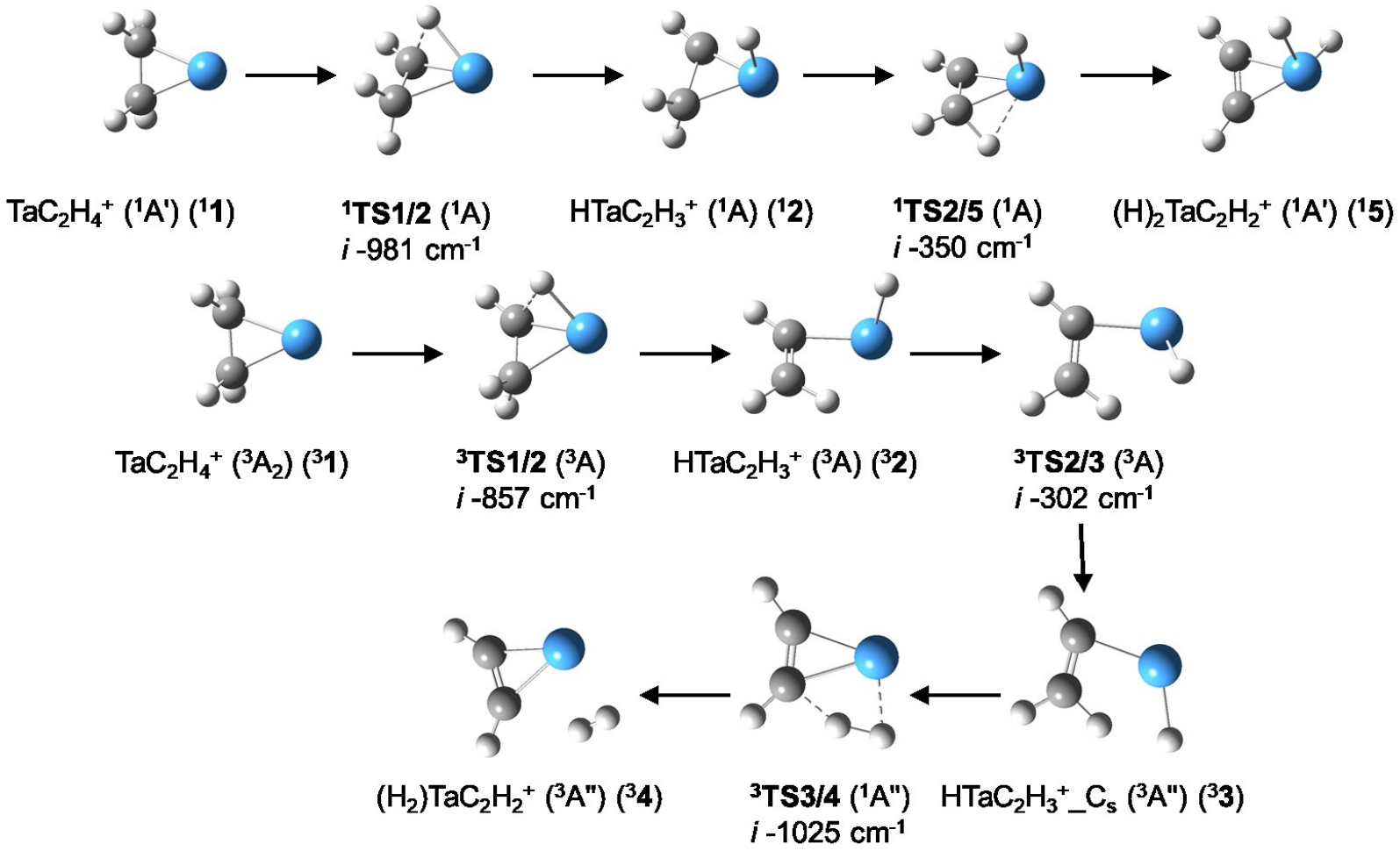
TaC2H4+ (1A') (1)
1TS1/2 (1A)
i -981 cm-1
HTaC2H3+ (1A) (2)
1TS2/5 (1A)
i -350 cm-1
(H)2TaC2H2+ (1A') (5)
TaC2H4+ (3A2) (3)
3TS1/2 (3A)
i -857 cm-1
HTaC2H3+ (3A) (2)
3TS2/3 (3A)
i -302 cm-1
(H2)TaC2H2+ (3A") (4)
3TS3/4 (1A")
i -1025 cm-1
HTaC2H3+_Cs (3A") (3)

Figure 3

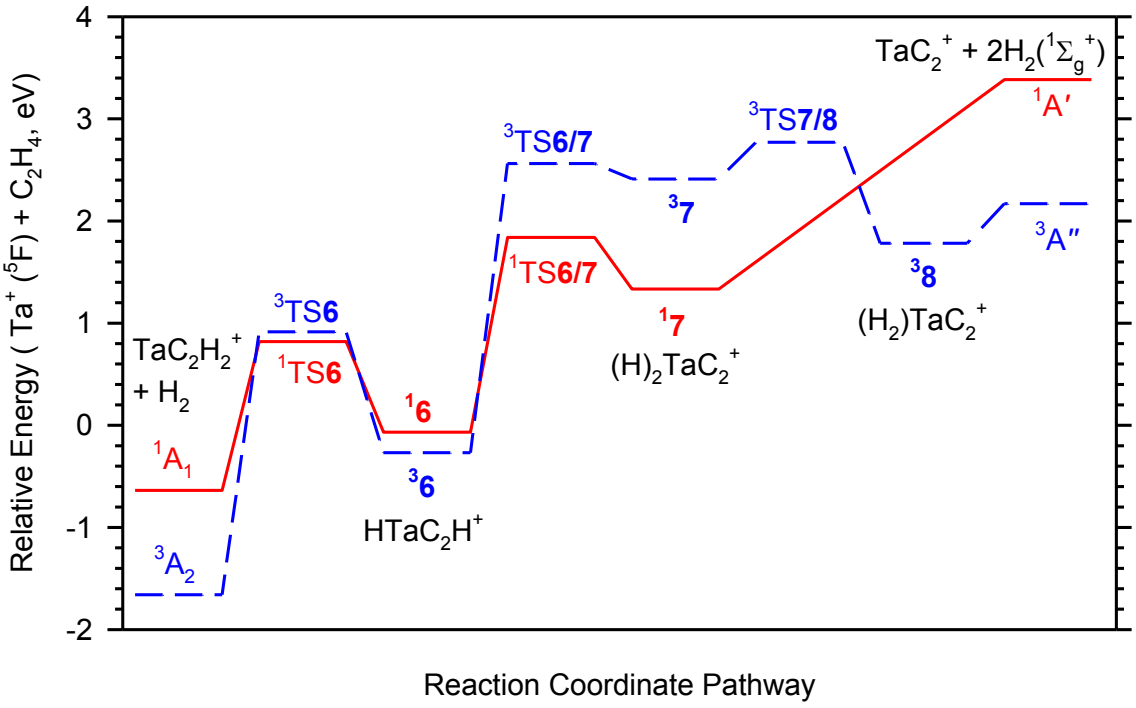

Figure 4

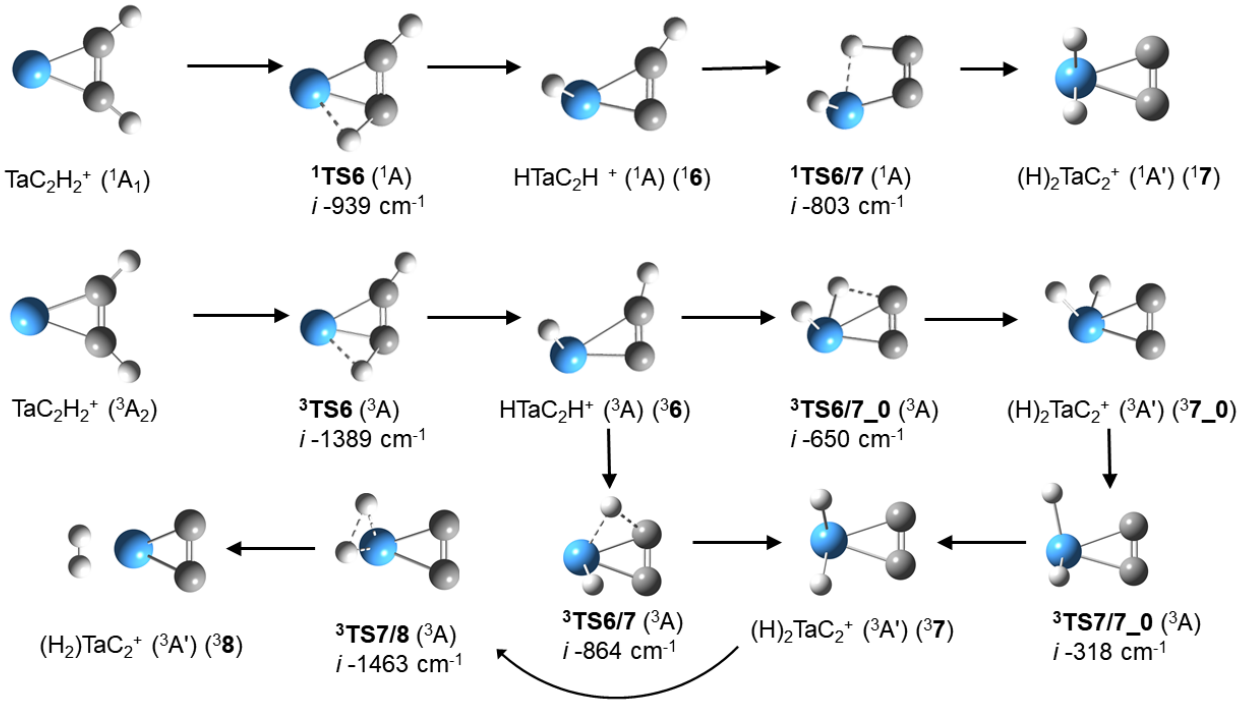

Figure 5

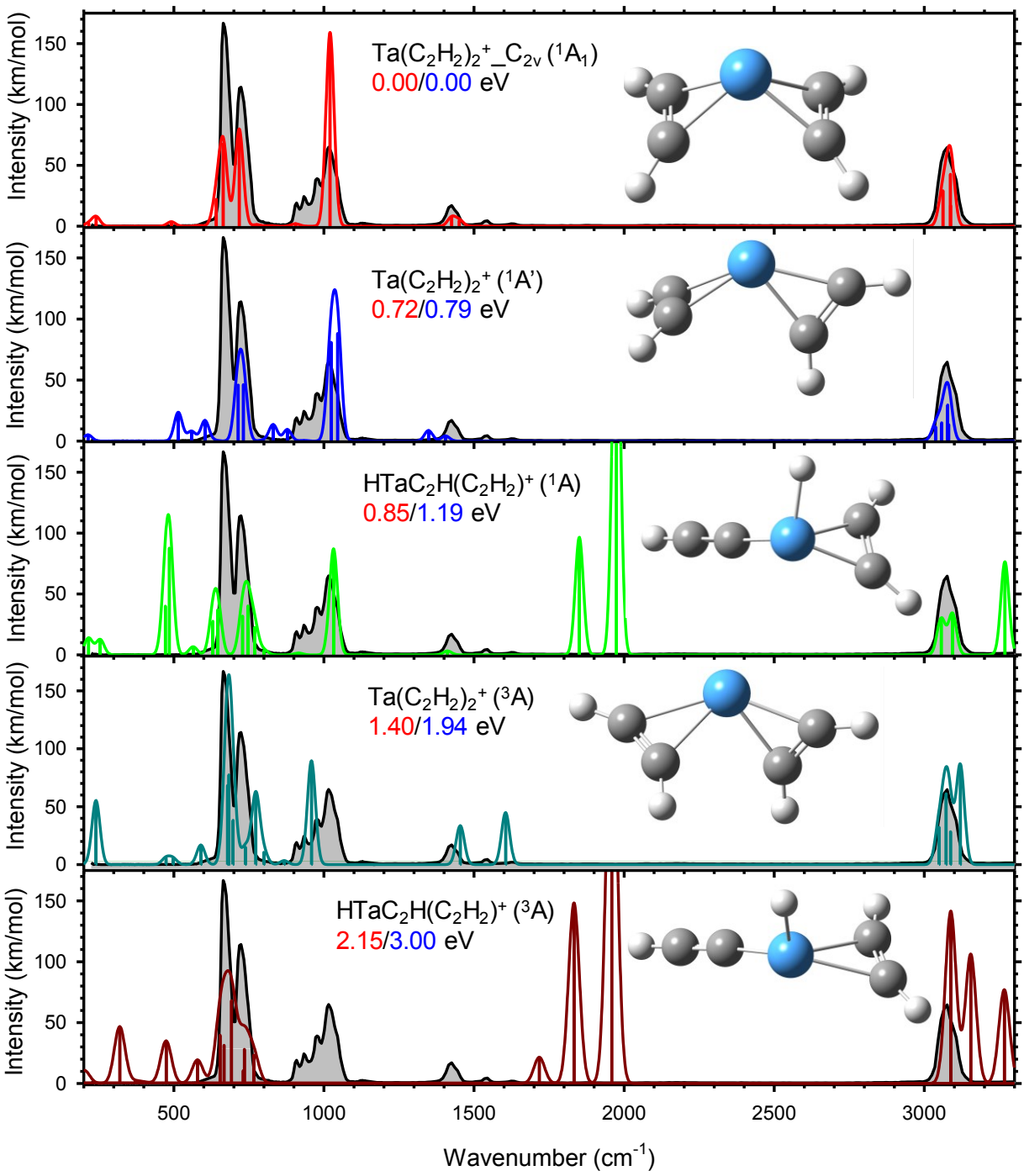
Ta(C2H2)2+_C2v (1A1)
0.00/0.00 eV
Ta(C2H2)2+ (1A')
0.72/0.79 eV
HTaC2H(C2H2)+ (1A)
0.85/1.19 eV
Ta(C2H2)2+ (3A)
1.40/1.94 eV
HTaC2H(C2H2)+ (3A)
2.15/3.00 eV
Intensity (km/mol)
Wavenumber (cm-1)

Figure 6

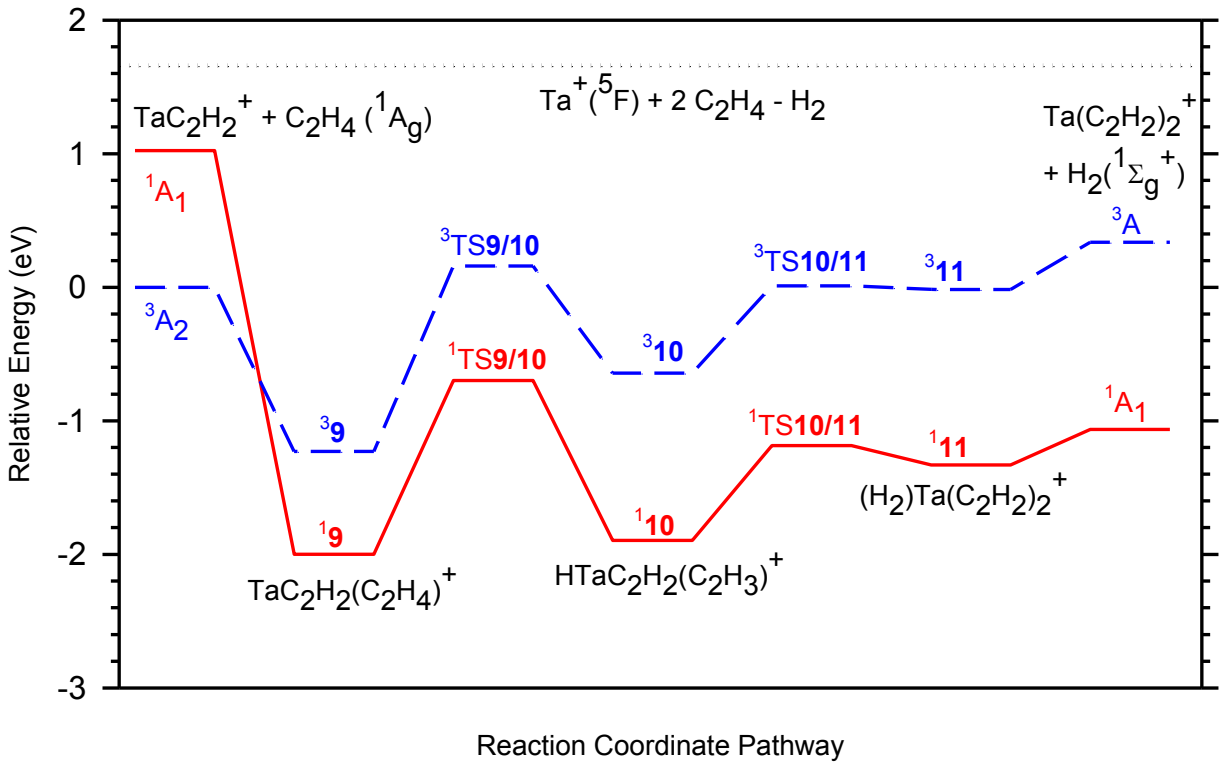

Figure 7

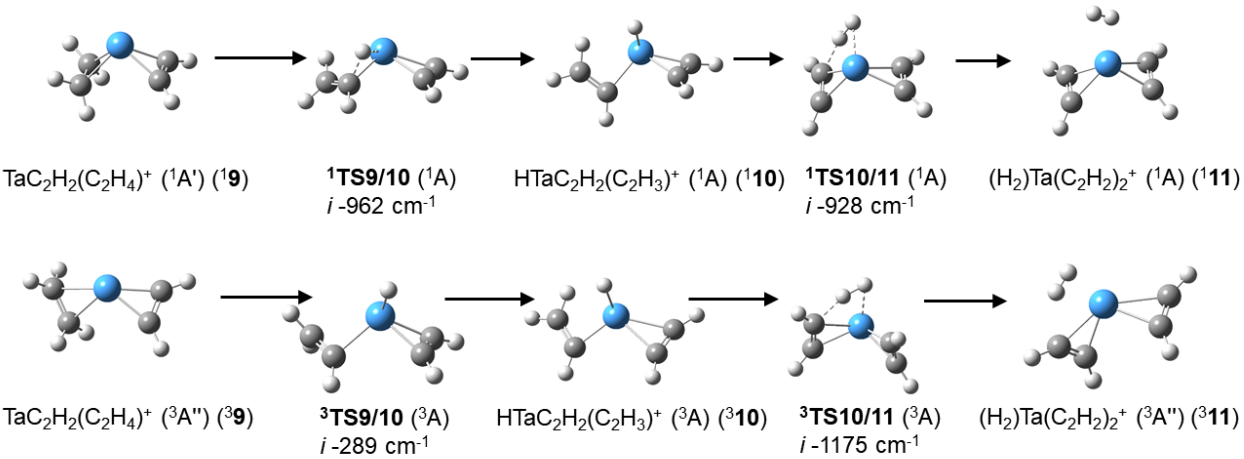

Figure 8

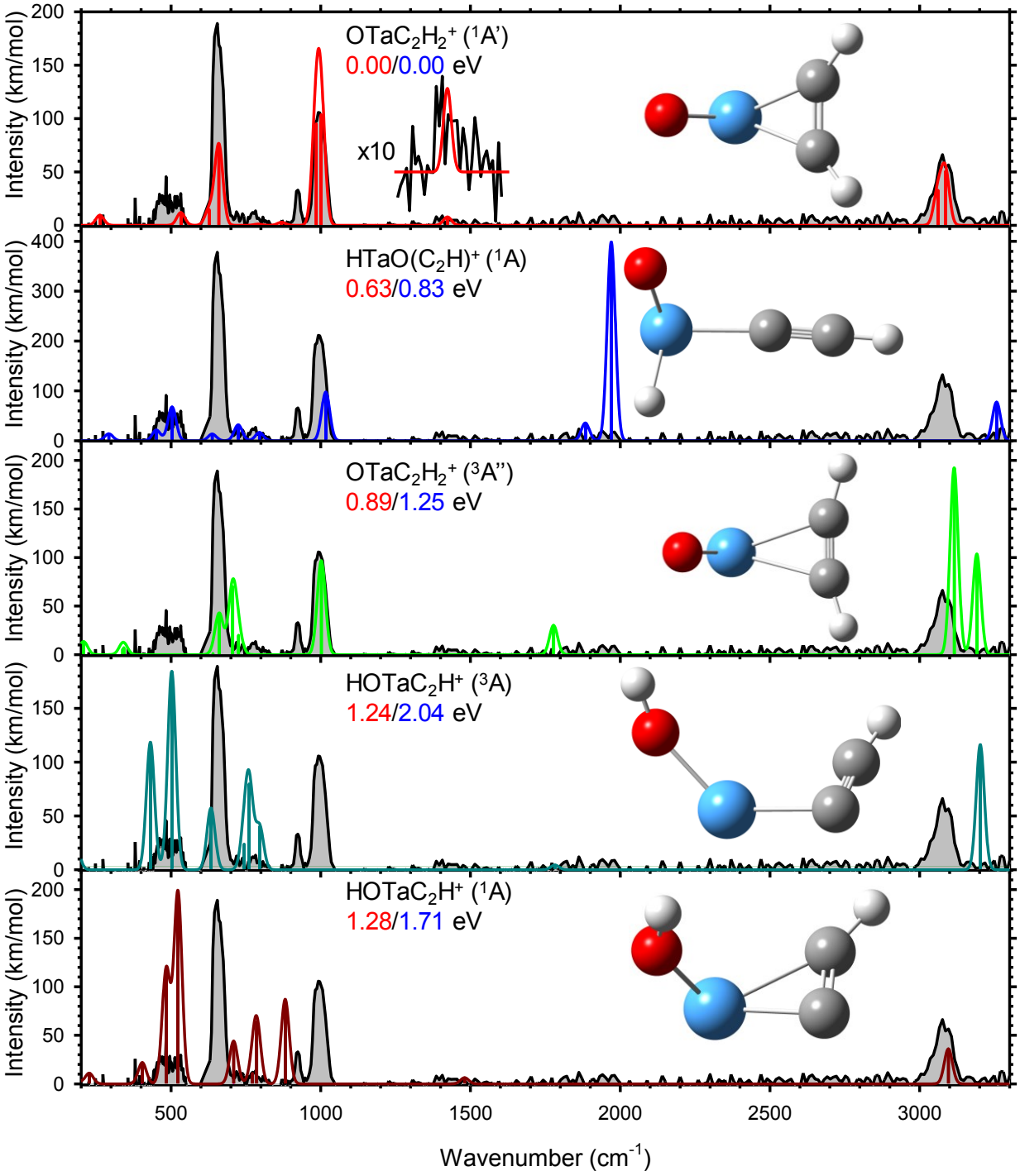
OTaC2H2+ (1A')
0.00/0.00 eV
x10
HTaO(C2H)+ (1A)
0.63/0.83 eV
OTaC2H2+ (3A'')
0.89/1.25 eV
HOTaC2H+ (3A)
1.24/2.04 eV
HOTaC2H+ (1A)
1.28/1.71 eV
Intensity (km/mol)
Wavenumber (cm-1)
500
1000
1500
2000
2500
3000

Figure 9

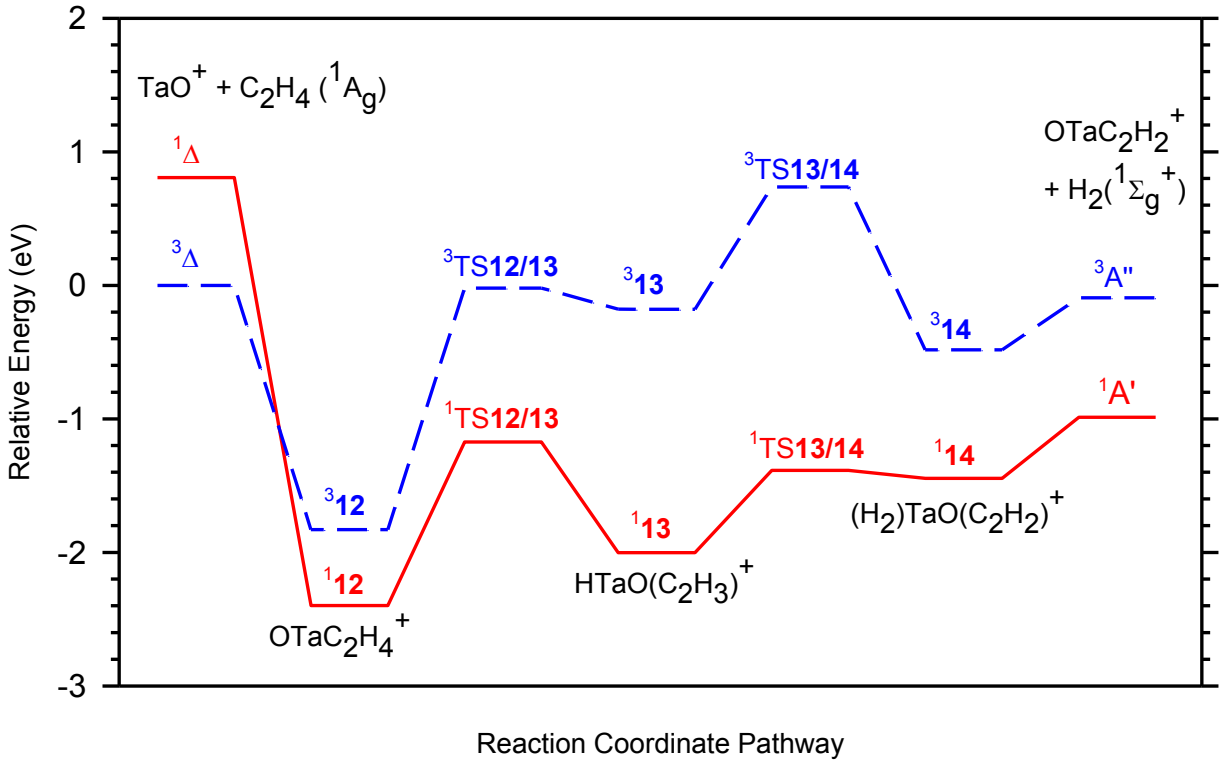

Figure 10

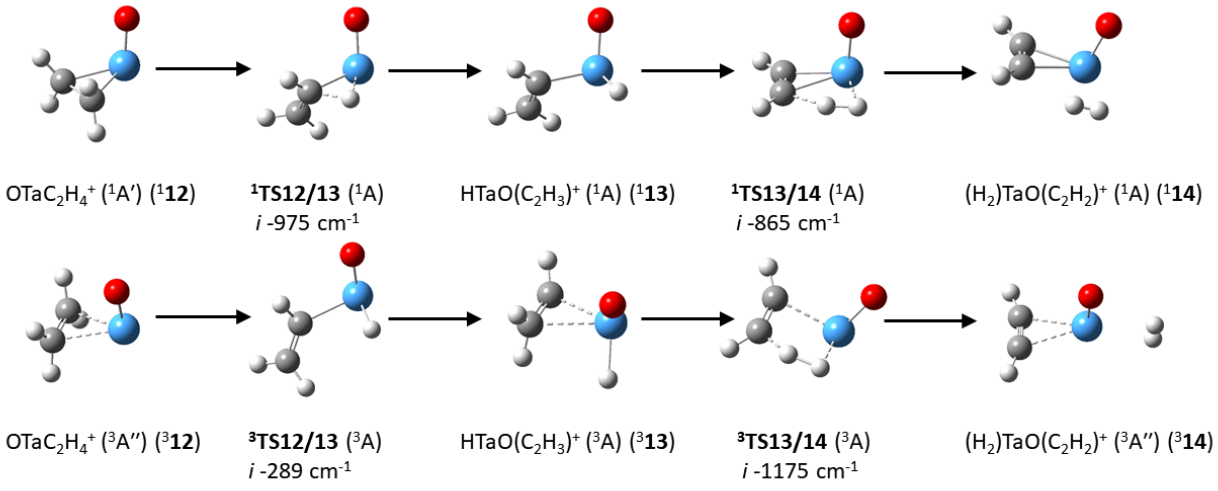

Figure 11